



Original Article

Irradiation damage in xenon-irradiated α -Al₂O₃ before and after annealingBingsheng Li^{a,b,*}, Huiping Liu^b, Long Kang^b, Tongmin Zhang^b, Lijun Xu^b, Anli Xiong^c^a State Key Laboratory for Environment-friendly Energy Materials, Southwest University of Science and Technology, Mianyang, Sichuan, 621010, China^b Institute of Modern Physics, Chinese Academy of Sciences, Lanzhou, Gansu, 730000, China^c Fundamental Science on Nuclear Wastes and Environmental Safety Laboratory, Southwest University of Science and Technology, Mianyang, Sichuan, 621010, China

ARTICLE INFO

Keywords:

Alumina

Irradiation damage

Microstructure

Raman spectroscopy

ABSTRACT

The irradiation damage build-up of α -Al₂O₃ under Xe²⁰⁺ ion irradiation has been investigated by a combination of Raman spectroscopy and transmission electron microscopy. α -Al₂O₃ crystalline was irradiated with 5 MeV Xe²⁰⁺ ions to fluences of $1 \times 10^{14} \text{ cm}^{-2}$, $5 \times 10^{14} \text{ cm}^{-2}$, $1 \times 10^{15} \text{ cm}^{-2}$ and $5 \times 10^{15} \text{ cm}^{-2}$ at room temperature. No amorphous phase was formed under the experimental condition. The Raman intensities of feature peaks of Al₂O₃ decrease after Xe ion irradiation. The interstitial-type dislocation loops with Burgers vectors of $b = 1/3 \langle 10\text{-}11 \rangle$ on the $\{10\text{-}10\}$ and (0001) habit planes were found. The formation of basal and prism dislocation loops is related to the lattice damage and position. After annealing, the Raman intensities of feature peaks of Al₂O₃ increases with annealing temperature. With annealing at 1500°C for 30 min, lattice defects were completely annealed out in the near surface region. Meanwhile, long dislocations and facet cavities on long dislocations were found in the Xe deposition region. Some lattice defects beyond the projected region were found due to the diffusion toward deep region during thermal annealing.

1. Introduction

Due to the advanced physicochemical stability, high electrical resistivity and high chemical inertness, alumina (Al₂O₃) is regarded as one of the important candidate ceramics materials used in fusion reactors, i.e., the window for a microwave heating system, an insulating material, optical windows and tritium permeation barriers [1,2]. Therefore, the effects of irradiation on α -Al₂O₃ have been studied in decades. The microstructural evolution of α -Al₂O₃ during neutron or ion irradiation has been widely studied. Neutron irradiation can induce the formation of interstitial dislocation loops with Burgers vectors of $b = 1/3 \langle 10\text{-}11 \rangle$ on both $\{10\text{-}10\}$ and (0001) habit planes [3]. Yamada et al. have investigated microstructure of α -Al₂O₃ pre-implanted with H, He, C and irradiated with Ar⁺ ions at 260–810°C and assumed the dislocation loops with (0001) and $\{1\text{-}100\}$ habit planes [4]. The number density of loops on the (0001) habit plane was higher than that on the $\{1\text{-}100\}$ planes. In addition, the influence of pre-implanted H, He and C on cavity distribution is not significant [4]. Zinkle and Pells have investigated microstructure of α -Al₂O₃ irradiated with Ar⁺ at 200 and 300 K. They found dislocation loops and network dislocations formed in α -Al₂O₃ under irradiation at 300 K. The values of step-height swelling are 4.5%, 3.5% and 2.8% after Ar⁺ irradiation to a dose of 10 dpa at 200 K, 300 K and 900 K, respectively [5]. Furuno et al.

have investigated radiation effects on α -Al₂O₃ irradiated with H₂⁺ ions at room temperature, 400°C, 650°C and 800°C [6]. Bubbles were found in the sample irradiated at room temperature. Below 400°C, dislocation loops and bubbles were homogeneously distributed. Above 650°C, bubbles are preferential to nucleate with the dislocation loops. Chen et al. have investigated microstructure of He-implanted α -Al₂O₃ after annealing. The majority loops with interstitial-type have habit planes of $\{10\text{-}10\}$ and (0001). Furthermore, the loops had a round shape on (0001) plane while some loops had a rectangular shape on $\{10\text{-}10\}$ planes. Bubbles associated with loops were formed after annealing at 1000°C [7]. The threshold dose for amorphization in α -Al₂O₃ is related to the irradiation temperature and ion species. Below 80 K, it needs a dose of 3–6 displacements per atom (dpa), while it needs over 100 dpa with implanted ion levels of on the order of 50 at.% during irradiation at room temperature [8,9].

Alumina can be also used in fission reactors, such as inert fuel host and rector components. Xenon is regarded as a major inert gas fission product, and it is worth studying xenon behavior in α -Al₂O₃. Up to now, xenon ion irradiation effects on α -Al₂O₃ have been less reported [10]. In this paper, we report the microstructure of lattice disorder in α -Al₂O₃ under xenon ion irradiations. The interstitial-type dislocation loops were investigated by conventional transmission electron microscopy and high resolution transmission electron microscopy. The type of Xe-

* Corresponding author at: State Key Laboratory for Environment-friendly Energy Materials, Southwest University of Science and Technology, Mianyang, Sichuan, 621010, China.

E-mail address: libingshengmvp@163.com (B. Li).

<https://doi.org/10.1016/j.jeurceramsoc.2019.05.035>

Received 17 March 2019; Received in revised form 17 May 2019; Accepted 20 May 2019

Available online 24 May 2019

0955-2219/© 2019 Elsevier Ltd. All rights reserved.

irradiation induced dislocation loops is related to the level of lattice damage and depth distribution. Most of lattice defects were recovered upon annealing at 1500°C for 30 min.

2. Experimental process

In the present study, the material is $\langle 0001 \rangle$ oriented $\alpha\text{-Al}_2\text{O}_3$ single-crystal wafers, which were obtained from MIT Company with a dimension of $10 \times 10 \times 0.5 \text{ mm}^3$. Xe^{20+} ions with an energy of 5 MeV were supplied by 320 kV High-voltage Platform in the Institute of Modern Physics, Chinese Academy of Sciences. The irradiation fluences were $1 \times 10^{14} \text{ cm}^{-2}$, $5 \times 10^{14} \text{ cm}^{-2}$, $1 \times 10^{15} \text{ cm}^{-2}$ and $5 \times 10^{15} \text{ cm}^{-2}$. The beam flux during irradiation was of the order of $10^{11} \text{ ions cm}^{-2}\text{s}^{-1}$ and the irradiation temperature was room temperature. Beam scanning was employed to achieve a uniform irradiation with an area of $15 \times 15 \text{ mm}^2$. The irradiation damage in dpa and concentration were simulated by SRIM-2008 quick cascade simulations using the displacement energies of O = 50 eV, Al = 20 eV, and density of 3.98 g/cm^3 [11]. Isochronal annealing was performed for 30 min under argon gas flow over the temperature range from 900°C to 1500°C.

Micro-Raman spectroscopy ($\mu\text{-RS}$) was employed to research the evolution of chemical bonds. $\mu\text{-RS}$ was performed using a Horiba Jobin Yvon HR-800 spectrometer at room temperature. The excitation wavelength was 532 nm from the Ar^+ laser and the laser spot was about 1 μm . The microstructure of the Xe irradiation-induced damage was studied by cross-sectional transmission electron microscopy (XTEM) and high resolution TEM (HRTEM) using a Tecnai G20 operated at 200 kV with a point resolution of 0.19 nm. The preparation process of the XTEM sample was mechanical thinning and then Ar^+ ion milling [12,13]. The sample was observed near the $[11\text{-}20]$ direction. The micrograph conditions were bright field (BF) and weak-beam dark field (WBDF). The distribution of defects under WBDF was counted with an uncertainty of about $\pm 20\%$. The thickness of the foils was determined by electron energy loss spectrum (EELS).

3. Results and discussion

3.1. As-implanted state

The Raman spectra of the $\alpha\text{-Al}_2\text{O}_3$ samples before and after irradiated by 5 MeV Xe^{20+} to fluences of $1 \times 10^{14} \text{ cm}^{-2}$, $5 \times 10^{14} \text{ cm}^{-2}$, $1 \times 10^{15} \text{ cm}^{-2}$ and $5 \times 10^{15} \text{ cm}^{-2}$ are illustrated in Fig. 1. The virgin Al_2O_3 normally known as corundum with Rc space group, presents seven Raman active phonon modes, $2A_{1g} + 5E_g$ (418 cm^{-1} and 648 cm^{-1} arise from A_{1g} (internal); 378 cm^{-1} , 432 cm^{-1} , 451 cm^{-1} , 755 cm^{-1} arise from E_g (external); 578 cm^{-1} arises from E_g (internal)) [14]. In the

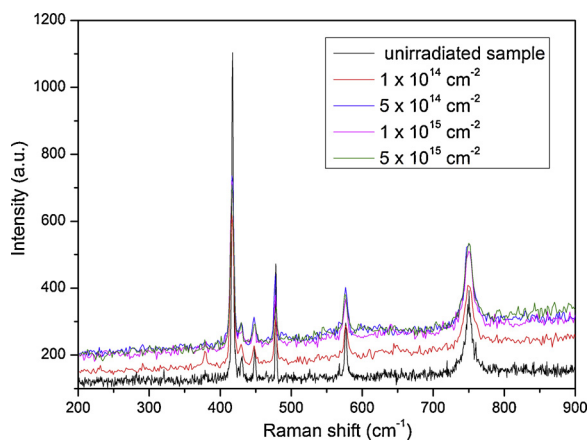


Fig. 1. Raman scattering spectra of Al_2O_3 before and after irradiated with 5 MeV Xe^{20+} to fluences of $1 \times 10^{14} \text{ cm}^{-2}$, $5 \times 10^{14} \text{ cm}^{-2}$, $1 \times 10^{15} \text{ cm}^{-2}$ and $5 \times 10^{15} \text{ cm}^{-2}$ at RT.

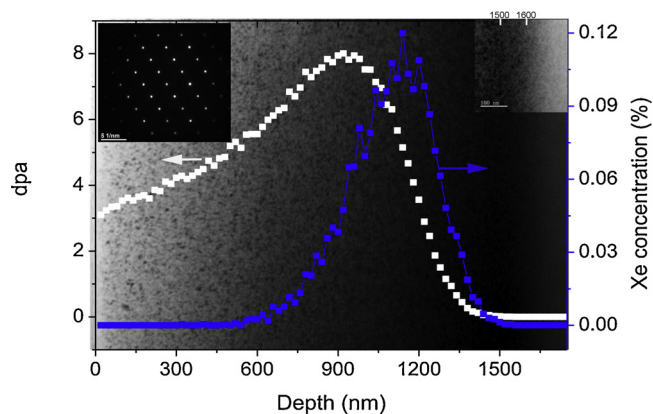


Fig. 2. XTEM bright field micrograph of Al_2O_3 irradiated with 5 MeV Xe^{20+} ions to a fluence of $5 \times 10^{15} \text{ He}^+/\text{cm}^2$ at RT, superposed the distribution of damage and helium deposition of the Xe irradiated GaN simulated by SRIM-2008. Electron diffraction pattern taken from the damaged layer and micrograph taken from the tail of the damage layer are shown as insets.

present experimental condition, the mode corresponding to A_{1g} at 648 cm^{-1} is not observed, while an extra band with peak at 478 cm^{-1} is observed. After Xe^{20+} ion irradiation, the background intensity increases due to the Rayleigh scattering from the defects induced by Xe^{20+} irradiation. The strong luminescence induces the raising baseline of spectrum. Furthermore, the intensities of Raman scattering peaks decrease with increasing the fluence. It is attributed to the increase of optical absorption induced by Xe^{20+} irradiation-induced defects. It should be noted that the Raman scattering peaks of Al_2O_3 can be still clearly observed in the sample irradiated with the maximum fluence. It indicates that the crystalline structure is remained under the present experimental condition.

The simulated profiles of the damage and xenon deposition of Al_2O_3 irradiated with 5 MeV Xe^{20+} ions with a fluence of $5 \times 10^{15}/\text{cm}^2$ superposed a XTEM view of the Xe^{20+} irradiated sample, as shown in Fig. 2. The electron diffraction pattern demonstrates the single crystal structure in the irradiation region, consistent with the result of Raman spectra. According to SRIM simulation, the mean projected region R_p is approximately 1130 nm with a straggling of ΔR_p is approximately 350 nm. The maximum damage is approximately 8 dpa. Dense black contrasts arising from Xe irradiation-induced dislocation loops, stacking faults and strain were observed. The damaged layer ranges from surface to a depth of 1650 nm and the irradiation damage is more serious at depths ranging from 1350 to 1650 nm. It is clearly shown that the SRIM-predicted Xe distribution and damage profiles are much shallower than that shown by the contrasted features in the XTEM image. Large discrepancies in the ion range between SRIM and experimental value is due to overestimation of electronic stopping power of the medium mass ions. Zhang et al. investigated Au^+ ion irradiation in GaN and argued a deviation of about 25% between the SRIM-predicted value and experimental value [15]. According to the defect contrast shown in Fig. 2, the damage peak appears located at a depth of 1500 nm, while the maximum Xe deposition is located at a depth of 1050 nm predicted by SRIM. There is a deviation of about 23%, consistent with Au^+ ion irradiation in GaN.

Fig. 3 presents weak beam dark field images of the damaged layer for the Xe^{20+} irradiated Al_2O_3 at room temperature. The images were taken along the $[11\text{-}20]$ zone axis. High densities of bright contrasts correlated to point defect clusters, dislocation loops, stacking faults and strains were observed. Rel-rod-streaks in the (0001) plane were presented in the electron diffraction pattern, as shown in the inset of Fig. 3(a). It indicates a very high density of dislocation loops located in the basal plane. Image taken under $g = 1\text{-}104$ condition, many dislocation loops exhibited edge-on contrast. It can be clearly visible some dislocation loops parallel to the basal plane but others perpendicular to

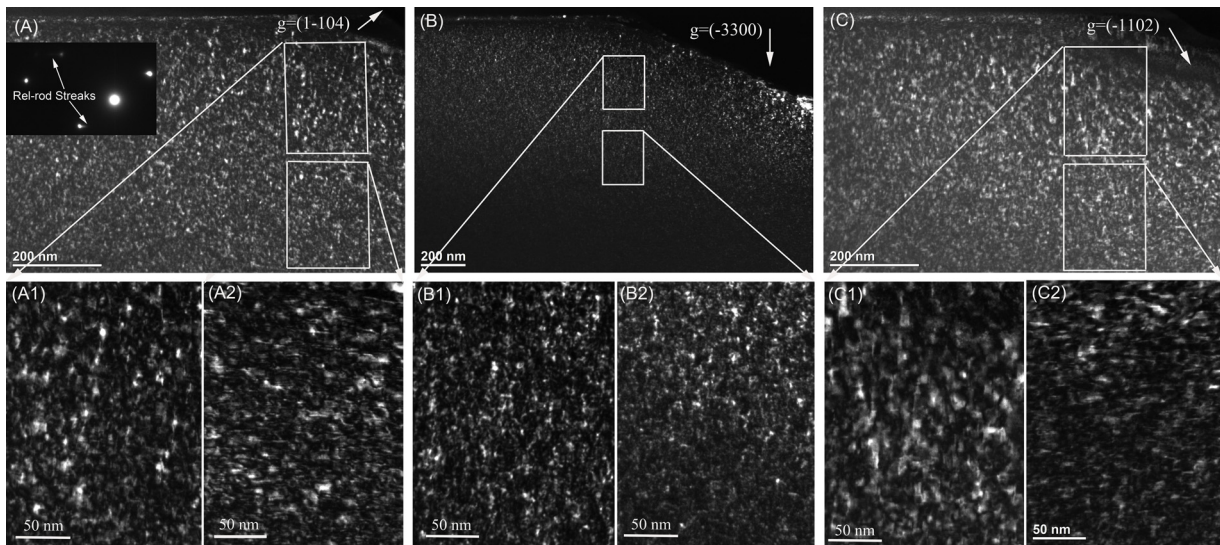


Fig. 3. XTEM weak beam dark field micrographs of Al₂O₃ irradiated with 5 MeV Xe²⁰⁺ to a fluence of $5 \times 10^{15} \text{ cm}^{-2}$ at RT. (A) $g = (1-104)$, (B) $g = (-3300)$ and (C) $g = (-1102)$. The bottom six images (A1 to C2) show the magnified images as marked in figures (A, B and C) respectively.

the implanted surface. More importantly, the majority of observed dislocation loops lying on the prism $\{1-100\}$ habit planes are located in the near surface region, as shown in Fig. 3(A1). However, the observed dislocation loops lying on the basal (0001) plane are located in the deep region, as shown in Fig. 3(A2). Image taken under $g = 3-300$ condition, a high density of point defect clusters and dislocation loops were observed in the damaged layer, as shown in Fig. 3(B). In the near surface region, the lattice defects exhibited large and bright contrasts compared to the lattice defects located in the deep region. It indicates that the sizes of observed lattice defects are larger in the near surface region than that in the deep region. Image taken under $g = -1102$ condition, the defect contrast is similar to the case of $g = 1-104$.

The size distributions of the lattice defects for two different diffraction factors are plotted in Fig. 4. Under $g = 1-104$, as shown in Fig. 4(a), the observed dislocation loops perpendicular to the implanted surface have a mean size of 8.11 nm and a number density of $3.7 \pm 0.7 \times 10^{22} \text{ cm}^{-3}$. The observed dislocation loops parallel to the basal plane have a mean size of 13.37 nm and a number density of $5.8 \pm 1.2 \times 10^{22} \text{ cm}^{-3}$. The dislocation loops on the basal plane are little larger than the dislocation loops on the prism planes. Under $g = 3-300$, as shown in Fig. 4(b), in the near surface region, the observed point defect clusters and dislocation loops have a mean size of 3.77 nm and a number density of $7.3 \pm 1.5 \times 10^{22} \text{ cm}^{-3}$. In the deep region, the observed point defect clusters and dislocation loops have a mean size of 3.13 nm and a number density of $1.4 \pm 0.3 \times 10^{23} \text{ cm}^{-3}$. In the deep region, the number density of observed lattice defects is larger than that in the near surface region. There are two reasons that can account for it.

One reason is that the surface acts as a strong sink for implantation-induced lattice defects, leading to the decrease in the number density of lattice defects in the near surface region. The other reason is that impurity due to Xe deposition can reduce the mobility of lattice defects, and thereby suppress the recombination of interstitials and vacancies, resulting in the increase in the number density of lattice defects in the Xe deposition region.

HRTEM was carried out to investigate atomic structure of dislocation loops on the prism planes and on the basal plane. The $[11-20]$ zone axis was chosen for the HRTEM observation. Fig. 5(a) shows a typical morphology of one basal dislocation loop located at between two prism dislocation loops. Lattice fringes are clearly visible and partial regions of lattice fringes are wavy due to lattice disorder. Fig. 5(b) shows Fourier-filtered HRTEM image and interstitial-type dislocation loops on the $(1-100)$ plane and (0006) plane were clearly visible. Pyramidal dislocations as well as their corresponding stacking faults were noted. The Burgers vectors of the pyramidal dislocation loops were $b = 1/3[1-101]$, as shown in Fig. 5(c). The $b = 1/3[1-101]$ can be regarded via the following reaction: $1/3[1-100] + 1/3[0001] \rightarrow 1/3[1-101]$. Partial zone containing observed basal dislocation loop and prism dislocation loops was magnified, as shown in Fig. 5(d). Interstitial-type basal dislocation loops on the (0006) plane and interstitial-type prism dislocation loops on the $(1-100)$ plane were visible. Fourier-filtered HRTEM image of Fig. 5(d) presents that the interstitial-type dislocation loops have Burgers vectors of $b = 1/3[1-101]$. In addition, the signal intensities of different lattice atoms of the basal dislocation loop on the $(1-104)$ plane and the prism dislocation loop on the $(1-10-2)$ plane

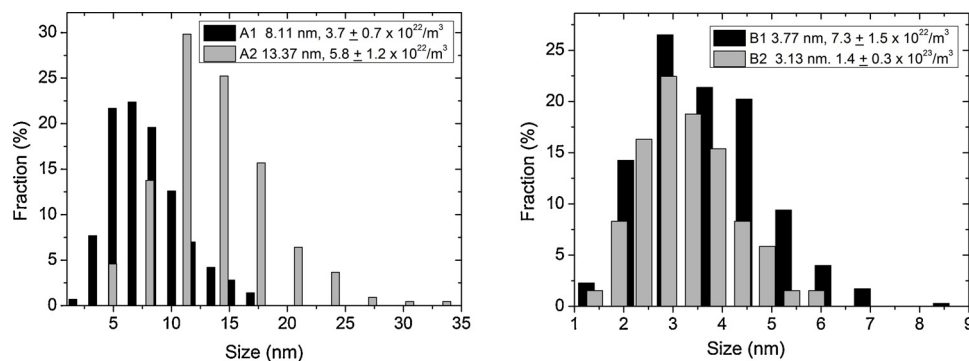


Fig. 4. Dislocation loop-size distributions for 5 MeV Xe²⁰⁺ ion-irradiated Al₂O₃ at RT observed under $g = (1-104)$ and $g = (3-300)$.

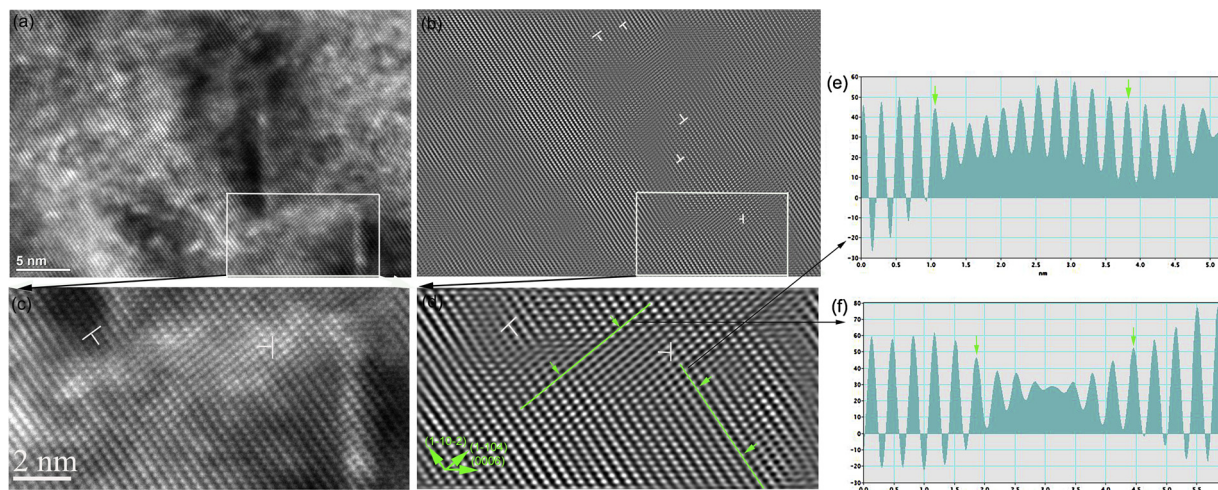


Fig. 5. HRTEM micrograph in the damaged layer, (a) showing the pyramidal plane dislocation loop and basal plane dislocation loop; (b) Fourier-filtered (0002) diffraction HRTEM image showing the pyramidal plane dislocation loops, prismatic plane dislocation loops and basal plane dislocation loops; (c) and (d) the magnified micrograph of the interstitial-type prismatic plane dislocation loop and basal dislocation loop as marked in figure (a) and (b) respectively; (e) and (f) the signal intensity of the analyzed atoms as indicated by one line across the prismatic plane dislocation loop and basal dislocation loop respectively.

were measured. One can clearly see that the signal intensities are quite low and signal peaks broadened for some lattice atoms. It indicates that the lattice atoms of the (1–104) and (1–10–2) planes occur shift under the formation of the basal dislocation loop and the prism dislocation loop, respectively.

Ions or neutron irradiation into alumina, irradiation induced the formation of interstitial dislocation loops with Burgers vectors of $b = 1/3 \langle 0001 \rangle$ lying on the (0001) plane and Burgers vectors of $b = 1/3 \langle 1-100 \rangle$ plane on the $\{1-100\}$ planes [7]. With increasing irradiation, these loops nucleate a shear partial dislocation with a Burgers vectors of $b = 1/3 \langle 10-11 \rangle$ lying on both the (0001) and $\{1-100\}$ planes. In the present study, the formation of prism dislocation loops and basal dislocation loops is related to lattice damage and position. Near the maximum damage layer, only basal dislocation loops were observed. Xe^{20+} ion irradiation produces dense Frenkel pairs, and interstitials are preferential to agglomerate on the basal plane. Therefore, basal dislocation loops are easy to nucleate in the maximum damage region. However, Xe impurity can reduce the mobility of interstitials, resulting in the sizes of basal dislocation loops that are too small to be found. Near the maximum damage region, one can see the basal dislocation loops with a high density and small sizes as compared to the case of away the maximum damage region. In the near surface region, surface acting as a sink for interstitials become significant. In this case, interstitials are preferential to migrate toward the sample surface, which can promote the nucleation of prism dislocation loops. In contrast to the ion-implanted GaN that the density of basal dislocation loops is far more than that of prism dislocation loops. It is related to a huge energy barrier for defect migration in GaN has been predicted by MD calculations [16], which can explain why it is hard to observe prism dislocation loops in GaN.

3.2. After annealing

Fig. 6 shows the Raman spectra of 5 MeV Xe^{20+} ions with the fluence of $5 \times 10^{15}/\text{cm}^2$ irradiated $\alpha\text{-Al}_2\text{O}_3$ after annealing at 900°C, 1200°C and 1500°C for 30 min. The intensities of Raman scattering peaks increase, while the background intensity decreases with increase in the annealing temperature, in particular, for the case of annealing at 1500°C that the baseline is almost the same with the un-irradiated sample. It indicates that the lattice defects were significantly annealed out during annealing at 1500°C. In order to verify this argument, a detailed TEM analysis of the sample irradiated at this fluence and then

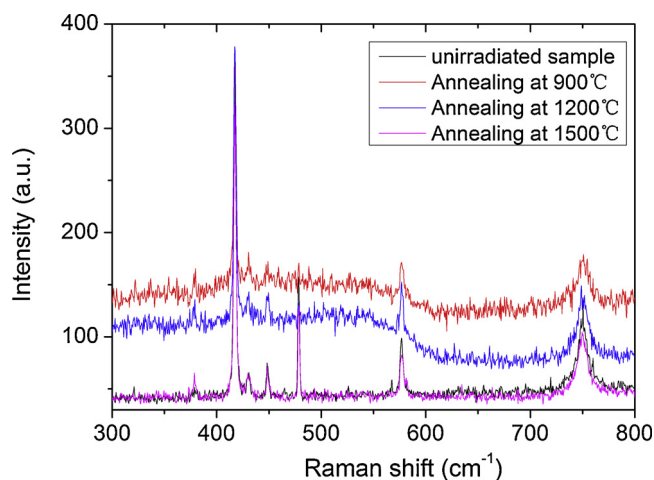


Fig. 6. Raman scattering spectra of Al_2O_3 before and after irradiated with 5 MeV Xe^{20+} to a fluence of $5 \times 10^{15} \text{ cm}^{-2}$ at RT followed by annealing at 900°C, 1200°C and 1500°C for 30 min.

annealed at 1500°C has been carried out.

Fig. 7 presents the over-viewed micrograph of the Xe-irradiated $\alpha\text{-Al}_2\text{O}_3$ after 1500°C annealing. There is an obvious damaged band located at depths ranging from 920 nm to about 1800 nm. The defect-denuded layer in the near surface region was clearly visible. It indicates dense lattice defects located in the near surface region that acting as a defect sink were annealed out during annealing at 1500°C. In the damaged band, the distributions of lattice defects and cavities are heterogeneous. In the middle of the damaged layer corresponding to the region between the damage peak and the maximum Xe deposition, isolated long dislocations with over 100 nm length were clearly observed, as shown in Fig. 7(b). In the vicinity of these long dislocations, no contrast was visible. It indicates that the long dislocations act as sink for lattice defects, leading to the annihilation of basal dislocation loops. In general, the binding energy per atom in a cluster increases with cluster size, so small clusters decompose to form large clusters at elevated temperature [17–21]. It is reasonable to state that basal dislocation loops would be disappeared, instead of long dislocations with increasing annealing time. In addition, Fig. 7(d) presents that the many faceted cavities prefer to grow on the long dislocations, because vacancies in the vicinity of long dislocation aggregate easily and lead to

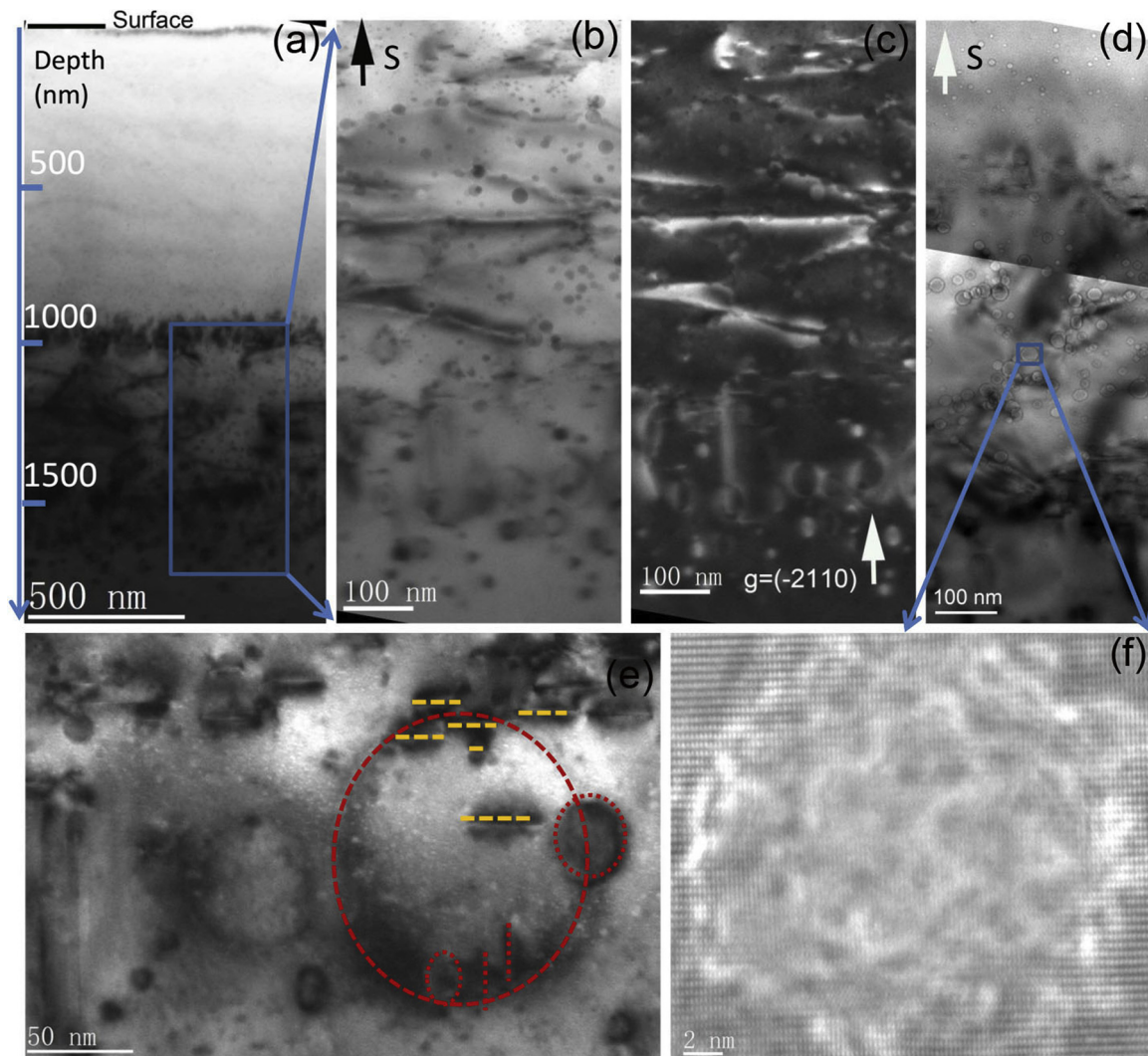


Fig. 7. XTEM bright field micrograph of Al_2O_3 irradiated with 5 MeV Xe^{20+} ions to a fluence of $5 \times 10^{15} \text{ He}^+/\text{cm}^2$ at RT followed by annealing at 1500°C for 30 min. (a) an over-viewed image of the damage distribution; (b) bright field image and (c) weak beam dark field with $g = (-2110)$ image of the dislocation lines and dislocation loops in the damaged layer; (d) under-focused view of cavities in the damaged layer; (e) the magnified micrograph showing basal and prism dislocation loops at the lower boundary of the damaged layer; (f) the magnified micrograph showing the cavity as marked in figure (d). The direction of the sample surface was noted.

faceted cavity formation due to the different free energies along the different crystal orientations [22–25]. The HRTEM micrograph presents the lattice fringes that are heavily disordered and only short-distance orders are visible on the cavity plane, as shown in Fig. 7(f). It indicates that the cavity exhibited over-pressurized state due to containing a very high density of Xe atoms. At the upper boundary of the damaged band, only basal dislocation loops were observed and some basal dislocation loops are of ~ 30 nm in diameter. Furthermore, cavities are smaller with a higher density in this region than that of the middle of the damaged band. However, at the lower boundary of the damaged band, very few of cavities close to the long dislocations were observed. Basal dislocation loops and prism dislocation loops were observed simultaneously. Some prism dislocation loops are of ~ 200 nm in diameter, as shown in Fig. 7(e). It can be seen that some basal dislocation loops attach with these large prism dislocation loops. Fig. 7(b) and (c) show that a narrow distribution of basal dislocation loops and a tail distribution of prism dislocation loops were visible, indicating that interstitials migrate toward deep region and accumulate in the $\{10\text{-}10\}$ planes, but not (0001) plane during the thermal annealing. It is the same case with the prism dislocation loops that are easily formed in the near surface region during Xe^{20+} ion irradiation at RT. The phenomenon of lattice defects

migration toward deep region has been observed in Si and MgO [26,27], but not in SiC and ZrO_2 [28,29]. It is related to a huge energy barrier for defect migration in SiC and ZrO_2 .

4. Conclusions

The damage processes formed in $\alpha\text{-Al}_2\text{O}_3$ under Xe^{20+} ion irradiation at RT and after thermal annealing were investigated by coupling the Raman spectroscopy and TEM. The intensities of Raman scattering decreases with increasing the fluence and no amorphous phase is formed upon Xe irradiation to 8 dpa. The interstitial-type dislocation loops with Burgers vectors of $b = 1/3 \langle 10\text{-}11 \rangle$ on the $\{10\text{-}10\}$ and (0001) habit planes were found. The lattice atoms of the $(1\text{-}104)$ and $(1\text{-}10\text{-}2)$ planes occur shift under the formation of the basal dislocation loop and the prism dislocation loop, respectively. Furthermore, the prism dislocation loops are easily formed in the near surface region and the basal dislocation loops are easily formed near the damage peak.

After annealing at 1500°C for 30 min, the recovery of lattice defects is significant. Prism dislocation loops formed in the near surface region are completely annealed out. In the damage peak, long dislocations and large faceted cavities formed on the long dislocations are observed.

Faceted cavities contain a very high density of Xe atoms. Many prism dislocation loops, but no cavities, migrate toward deep region.

Acknowledgements

The work was supported by National Nature Science Foundation of China (Grant Nos.11475229, U1832133) and the Doctor Research Foundation of Southwest University of Science and Technology (Grant No. 18zx7141). The authors appreciate the Laboratory of 320 kV High-voltage Platform in Institute of Modern Physics, CAS for Xenon irradiation and Dr. Xu Lijun for TEM observation.

References

- [1] S. Yamamoto, T. Shikama, V. Belyakov, E. Farnum, E. Hodgson, T. Nishitani, D. Orlinski, S. Zinkle, S. Kasai, P. Stott, K. Young, V. Zaveriaev, A. Costley, L. Dekock, C. Walker, G. Janeschitz, Impact of irradiation effects on design solutions for ITER diagnostics, *J. Nucl. Mater.* 283-287 (2000) 60–69.
- [2] F.W. Clinard Jr., Ceramics for fusion devices, *J. Mater. Eng. Syst.* 6 (1984) 100–106.
- [3] F.W. Clinard Jr., G.F. Hurley, L.W. Hobbs, Neutron irradiation damage in MgO, Al₂O₃ and MgAl₂O₄ ceramics, *J. Nucl. Mater.* 108-109 (1982) 655–670.
- [4] R. Yamada, S.J. Zinkle, G.P. Pells, Microstructure of Al₂O₃ and MgAl₂O₄ pre-implanted with H, He, C and irradiated with Ar⁺ ions, *J. Nucl. Mater.* 209 (1994) 191–203.
- [5] S.J. Zinkle, G.P. Pells, Microstructure of Al₂O₃ and MgAl₂O₄ irradiated at low temperatures, *J. Nucl. Mater.* 253 (1998) 120–132.
- [6] S. Furuno, N. Sadajima, K. Hojou, K. Izui, H. Otsu, T. Matsui, Radiation effects on Al₂O₃ irradiated with H₂⁺ ions, *J. Nucl. Mater.* 258-263 (1998) 1817–1821.
- [7] J. Chen, Z.Y. He, P. Jung, Microstructure of helium-implanted α -Al₂O₃ after annealing, *Acta Mater.* 54 (2006) 1607–1614.
- [8] H. Abe, S. Yamamoto, H. Naramoto, Amorphization in aluminum oxide induced by ion irradiation, *Nucl. Instr. Meth. B* 127-128 (1997) 170–175.
- [9] C.W. White, C.J. Mehargue, P.S. Sklad, L.A. Boatner, G.C. Farlow, Ion implantation and annealing of crystalline oxides, *Mater. Sci. Rep.* 4 (1989) 41–146.
- [10] H. Zirour, M. Izerrouken, A. Sari, Radiation damage induced in Al₂O₃ single crystal sequentially irradiated with reactor neutrons and 90 MeV Xe ions, *Nucl. Instr. Meth. B* 377 (2016) 105–111.
- [11] www.srim.org.
- [12] B.S. Li, Z.G. Wang, Structures and optical properties of H₂⁺-implanted GaN epilayers, *J. Phys. D Appl. Phys.* 48 (2015) 225101-225012.
- [13] Y.Z. Liu, B.S. Li, H. Lin, L. Zhang, Recrystallization phase in He-implanted 6H-SiC, *Chin. Phys. Lett.* 34 (2017) 076101–076104.
- [14] A. Misra, H.D. Bist, M.S. Navati, R.K. Thareja, J. Narayan, Thin film of aluminum oxide through pulsed laser deposition: a micro-Raman study, *Mater. Sci. and Eng. B* 79 (2001) 49–54.
- [15] Y.W. Zhang, M. Ishimaru, J. Jagielski, W.M. Zhang, Z.H. Zhu, L.V. Saraf, W.L. Jiang, L. Thome, W.J. Weber, Damage and microstructure evolution in GaN under Au ion irradiation, *J. Phys. D Appl. Phys.* 43 (2010) 085303–085311.
- [16] J. Nord, K. Nordlund, J. Keinonen, Molecular dynamics study of damage accumulation in GaN during ion beam irradiation, *Phys. Rev. B* 68 (2003) 184104–184110.
- [17] J. Chen, P. Jung, H. Trinkaus, Microstructural evolution of helium-implanted α -SiC, *Phys. Rev. B* 61 (2000) 12923–12932.
- [18] Y.Z. Liu, B.S. Li, L. Zhang, High-temperature annealing induced He bubble evolution in low energy He ion implanted 6H-SiC, *Chin. Phys. Lett.* 34 (2017) 052801–052804.
- [19] J.J. Sun, B.S. Li, Y.W. You, J. Hou, Y.C. Xu, C.S. Liu, Q.F. Fang, Z.G. Wang, The stability of vacancy clusters and their effect on helium behavior in 3C-SiC, *J. Nucl. Mater.* 503 (2018) 271–278.
- [20] K. Wang, M.E. Bannister, F.W. Meyer, C.M. Parish, Effect of starting microstructure on helium plasma-materials interaction in tungsten, *Acta Mater.* 124 (2017) 556–567.
- [21] B.S. Li, C.H. Zhang, H.H. Zhang, T. Shibayama, Y.T. Yang, Study of the damage produced in 6H-SiC by He irradiation, *Vacuum* 86 (2011) 452–456.
- [22] W.T. Han, H.P. Liu, B.S. Li, Transmission electron microscopy and high-resolution electron microscopy studies of structural defects induced in Si single crystals implanted by helium ions at 600°C, *Appl. Surf. Sci.* 455 (2018) 433–437.
- [23] S. Kondo, C.M. Parish, T. Koyanagi, Y. Katoh, Equilibrium shapes and surface selection of nanostructures in 6H-SiC, *Appl. Phys. Lett.* 110 (2017) 142106–142111.
- [24] B.S. Li, Y.Y. Du, Z.G. Wang, The effects of swift heavy-ion irradiation on helium-ion-implanted silicon, *Nucl. Instr. Meth. B* 337 (2014) 21–26.
- [25] Q. Shen, W. Zhou, G. Ran, R.X. Li, Q.J. Feng, N. Li, Evolution of helium bubbles and discs in irradiated 6H-SiC during post-implantation annealing, *Materials* 10 (2017) 101–108.
- [26] B.S. Li, C.H. Zhang, Y.T. Yang, L.Q. Zhang, C.L. Xu, Microstructure evolution upon annealing in Ar-implanted Si, *Appl. Surf. Sci.* 257 (2011) 9183–9187.
- [27] S. Moll, Y. Zhang, A. Debelle, L. Thome, J.P. Crocombette, Z. Zihua, J. Jagielski, W.J. Weber, Damage processes in MgO irradiated with medium-energy heavy ions, *Acta Mater.* 88 (2015) 314–322.
- [28] W.T. Han, B.S. Li, Microstructure defects in He-irradiated polycrystalline α -SiC at 1000°C, *J. Nucl. Mater.* 504 (2018) 161–165.
- [29] S. Moll, L. Thome, G. Sattonnay, A. Debelle, F. Garrido, L. Vincent, J. Jagielski, Multistep damage evolution process in cubic zirconia irradiated with MeV ions, *J. Appl. Phys.* 106 (2009) 073509–073517.